

New Insights into the Correlation between Morphology, Excited State Dynamics, and Device Performance of Small Molecule Organic Solar Cells

Guankui Long, Bo Wu, Ankur Solanki, Xuan Yang, Bin Kan, Xinfeng Liu, Dongchang Wu, Zhou Xu, Wei-Ru Wu, U-Ser Jeng, Jinyou Lin, Miaomiao Li, Yunchuang Wang, Xiangjian Wan, Tze Chien Sum,* and Yongsheng Chen*

Morphology plays a vital role on the performance of organic photovoltaics. However, our understanding of the morphology-performance relationships for organic photovoltaics remains lacking. Specifically, it is still an open question why some bulk-heterojunction blends exhibit electric field dependent $J-V$ curves, while others do not. Through detailed fs- μ s transient absorption spectroscopy and morphology studies on the representative bulk-heterojunction type small molecule (SM) donor system, a picture of different $J-V$ behaviors from morphology aspects and excited dynamics is revealed. Our findings reveal that amorphous morphology in the lack of percolated pathways leads to the formation of strongly bound charge transfer states (CTSs), which accounts for about one third of the photoexcited species. Therefore, field-dependent $J-V$ curves are obtained as these CTSs mainly undergo geminate recombination or function as interfacial traps for nongeminate recombination. On the other hand, the CTSs are totally suppressed after post-treatment owing to the formation of bicontinuous morphology, which results in very high efficiencies from exciton generation, diffusion, dissociation to charge extraction, thus contributes to field-independent $J-V$ characteristics. The insights gained in this work provide the effective guidelines to further optimize the performance of bulk-heterojunction type SM-organic photovoltaics through judicious morphology control and engineering.

1. Introduction

Power conversion efficiencies (PCEs) of solution-processed polymer organic photovoltaics (P-OPVs) have steadily improved due to the progressive developments in molecular design^[1–7] and device optimization with novel device structures and carefully control of the active layer morphology.^[8–12] PCEs exceeding 10% have recently been achieved.^[8,13–17] Concurrently, small molecule-based OPVs (SM-OPVs)^[18–23] have also moved forward with PCEs on par with their P-OPV counterparts.^[24–28] Compared to P-OPVs, SM-OPVs possess some distinct advantages of having well-defined molecular structures, intrinsic monodispersity, high purity, more easily controlled energy levels, less batch to batch variation, etc.^[24,29–37] From the extensive morphology^[38–44] and the excited state dynamics^[45–50] studies performed, it was established that the active layer morphology in OPVs has a profound influence on the photophysical processes

Dr. G. Long, X. Yang, B. Kan, M. Li, Y. Wang, Dr. X. Wan, Prof. Y. Chen
State Key Laboratory and Institute of Elemento-Organic Chemistry
Collaborative Innovation Center of Chemical Science
and Engineering (Tianjin)
School of Materials Science and Engineering
Nankai University
Tianjin 300071, China
E-mail: yschen99@nankai.edu.cn

Dr. B. Wu, A. Solanki, Dr. X. Liu, Prof. T. C. Sum
Division of Physics and Applied Physics
School of Physical and Mathematical Sciences (SPMS)
Nanyang Technological University (NTU)
21 Nanyang Link 637371, Singapore
E-mail: tzechien@ntu.edu.sg

Dr. B. Wu
Singapore-Berkeley Research Initiative for Sustainable
Energy (SinBeRISE)
1 Create Way, Singapore 138602, Singapore

D. Wu, Dr. Z. Xu
Shanghai Nanoport
FEI Trading (Shanghai) Co., Ltd.
Shanghai 201210, China

Dr. W.-R. Wu, Prof. U.-S. Jeng
National Synchrotron Radiation Research Center
101 Hsin-Ann Road, Science-Based Industrial Park
Hsinchu 30077, Taiwan

Dr. W.-R. Wu, Prof. U.-S. Jeng
Chemical Engineering Department
National Tsing-Hua University
Hsinchu 30013, Taiwan

Prof. J. Lin
Shanghai Synchrotron Radiation Facility
Shanghai Institute of Applied Physics
Chinese Academy of Sciences
Shanghai 201204, China



DOI: 10.1002/aenm.201600961

of exciton (EX) generation, diffusion, dissociation, charge transport, collection processes, and consequently the device performance.^[51–57] Despite the tremendous progresses have been made on elucidating the photophysical process and device performance, there are still gaps in our understanding of the structure-performance relationship between the active layer morphology, excited state dynamics and device performance for OPVs. Specifically, it is still puzzling from morphology considerations why some bulk heterojunction (BHJ) blends exhibit electric field dependent J - V curves, while others do not. The origin of different J - V behaviors is still an open question, which involves a complex interplay of the factors of electric field dependent charge generation, extraction, and the active layer morphology.^[57,58] One possible approach to decouple the sensitive morphology influence is to utilize small molecule donors with well-defined molecular structures.

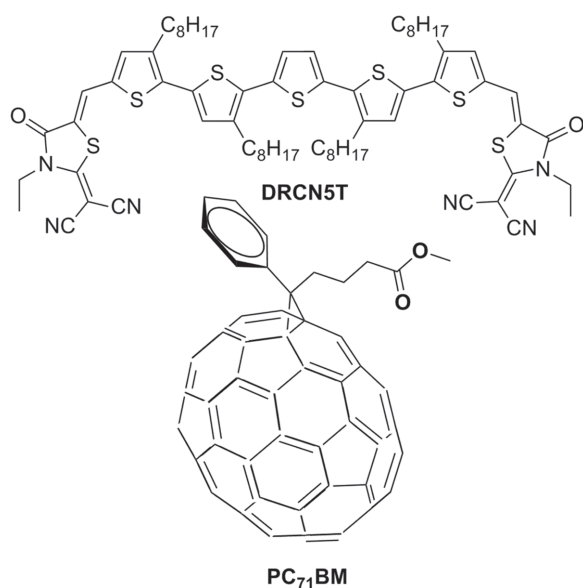
Herein, we present a systematic study on one of the representative BHJ type small molecule donor systems **DRCN5T** (2,2'-((5Z,5'Z)-5,5'-((3,3''',3''',4'-tetraoctyl-[2,2':5',2'':5'',2'':5''',2'':5''',2''':5''',2''':5''')-quinquethiophene]-5,5''''-diyl)-bis(methanylylidene))bis(3-ethyl-4-oxothiazolidine-5,2-diylydene)dimalononitrile, the chemical structure is shown in **Scheme 1**):PC₇₁BM ([6,6]-phenyl-C₇₁-butyric acid methyl ester) bulk heterojunction system using fs- μ s transient absorption (TA) spectroscopy correlated with morphologies, photophysical processes, and device performance. We are seeking to establish the clear relationships between active layer morphology, excited state dynamics, and device performance in SM-OPVs to guide the morphology control and device optimization toward the goal of the final commercialization. A large population of strongly bound charge transfer states (CTSs) were formed in the amorphous BHJ blend that does not contribute to the photocurrent. These states then mainly undergo geminate recombination within several nanoseconds or function as interfacial traps that accelerate the nongeminate recombination of charge carriers. As these CTSs could only be dissociated and extracted by applying very large reverse voltages,^[24,57–59] field-dependent J - V

curves were thus obtained from this amorphous morphology. In contrast, the strongly bounded CTSs were almost totally absent in the post-treated samples owing to the formation of the crystallized fibrillar morphology. This bicontinuous donor:acceptor network acts as “highways” for the excitons (EX) efficiently diffuse to the interfaces for dissociation, and then the separated charges were transported and extracted by the built-in potential with nearly 100% yields. The ratio between the CTSs and polaron populations are 1:2.1 and 1:4.5 for the as-cast and post-treated films, respectively, which verifies that the exciton dissociation efficiency increases significantly from \approx 68% for the as-cast film to \approx 82% after post-treatment.

2. Results and Discussion

2.1. Morphology Analysis

For **DRCN5T**:PC₇₁BM-based OPV devices, field dependent J - V curve with PCE of 3.31% in the as-cast state and field independent J - V curve with PCE of 10.08% was obtained after combining post-thermal annealing and solvent vapor annealing (Figure S1, Supporting Information). To understand the origin of the sharp differences of the device performance before and after post-treatment, the morphology of the active layers was first investigated by transmission electron microscopy (TEM), bright-field (BF), and dark-field (DF) scanning transmission electron microscopy (STEM). **Figure 1a,b** shows the TEM bright-field images of **DRCN5T**:PC₇₁BM blend films before and after post-treatment, and the morphology of the blend films without or with post-treatment is totally different. In the as-cast **DRCN5T**:PC₇₁BM blend film, the PC₇₁BM clusters are well dispersed in the amorphous **DRCN5T** matrix and very small grains of **DRCN5T** or PC₇₁BM are finely mixed together. This amorphous donor and aggregated acceptor type morphology is further confirmed by the BF- and DF-STEM measurements (Figure 1c,e), respectively. Such amorphous morphology at the nanoscales lacks in percolated pathways to the electrodes and thus facilitates the formation of strongly bounded CTSs. On the other hand, a much clearer nanoscale phase separation and bicontinuous network with the “fibrillar”-like morphology (the fiber width at approximately 18 ± 2 nm) was observed over the entire area for the **DRCN5T**:PC₇₁BM blend film after post-treatment (Figure 1b). The BF- and DF-STEM images for the post-treated blend film are shown in Figure 1d,f, the clearly bicontinuous donor networks combined with stronger fullerene domains are observed. From the above TEM, BF- and DF-STEM results, it is concluded that amorphous donor matrix with well dispersed fullerene clusters dominates in the as-cast **DRCN5T**:PC₇₁BM blends, which evolves into bicontinuous network with crystallized fibrillar morphology after post-treatment. Such networks could act as “highways” for the efficient exciton diffusion and charge extraction, thus would contribute to the enhanced device performance. This crystallized fibrillar morphology after post-treatment was further verified by the topographic images (Figure 1g,h) and phase-contrast images (Figure S2, Supporting Information) using atomic force microscopy (AFM).



Scheme 1. The chemical structure of the **DRCN5T** and PC₇₁BM.

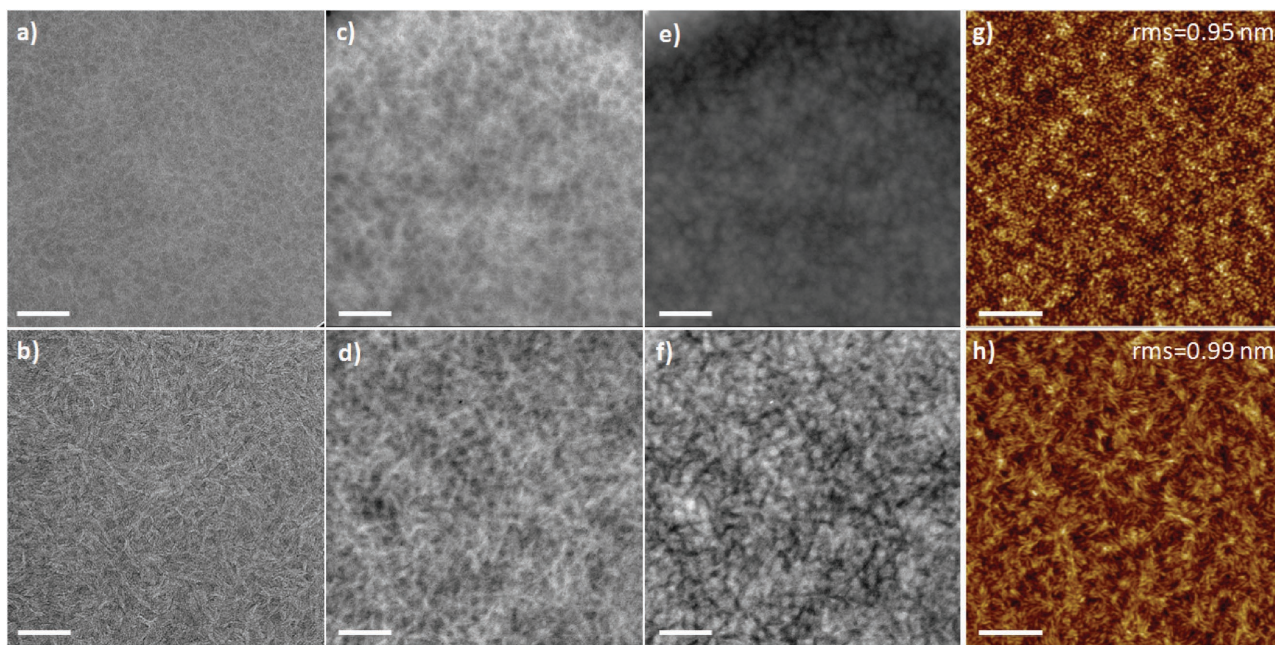


Figure 1. TEM bright-field images of the as-cast a) and post-treated b) **DRCN5T:PC₇₁BM** blend films. Bright-field STEM images of the as-cast c) and post-treated d) **DRCN5T:PC₇₁BM** blend films. Dark-field STEM images of the as-cast e) and post-treated f) **DRCN5T:PC₇₁BM** blend films. AFM phase-contrast images of the as-cast g) and post-treated h) **DRCN5T:PC₇₁BM** blend films, respectively. The scale bars are 200 nm in (a–f), and 1 μm in (g–h).

2.2. Grazing Incidence Wide-Angle X-Ray Scattering (GIWAXS) and Grazing Incidence Small-Angle X-Ray Scattering (GISAXS)

The crystallinity of the **DRCN5T** domains and the size of **PC₇₁BM** clusters in the as-cast and post-treated films were further investigated by the GIWAXS. As shown in Figure S3 (Supporting Information), a strong (100) scattering peak was observed in the pristine **DRCN5T** film ($q = 0.34 \text{ \AA}^{-1}$, $d_{100} = 18.48 \text{ \AA}$), while the scattering intensity of this peak was significantly enhanced after post-treatment. The crystal domain size along the (100) direction also increases from 19.80 nm in the as-cast **DRCN5T** film to 26.19 nm after post-treatment. This indicates the crystallinity of the **DRCN5T** molecules is further enhanced after post-treatment, consistent with the enhancement and redshift of the UV–vis absorption spectra as discussed below. On the contrary, the (100) peak is totally diminished after blending with **PC₇₁BM** (as shown in Figure 2a,c), further confirming that the crystalized **DRCN5T** domains are completely disrupted by fullerene acceptors. After further post-treatment of the blend film, the (100) peak is reproduced and well oriented particularly at $q_z = 0.34 \text{ \AA}^{-1}$ in the vertical direction along q_z (scattering wavevector component along the film surface normal). The corresponding crystal domain size along this (100) direction is estimated to be 19.01 nm, which is also consistent with the morphology results from TEM and STEM as discussed above. The GIWAXS patterns and the corresponding profiles in Figure 2 are corrected for pole figures.^[38] Since the first diffraction peak position is relatively low ($q_z = 0.34 \text{ \AA}^{-1}$), the crystal domains size extracted from the nominal edge-on (100) peak width (Figure 2c) would only be marginally ($\approx 20\%$) smaller than that for truly edge-on crystals as shown previously.^[60–62]

The GISAXS was also performed on both pure **DRCN5T** films and their BHI blends with **PC₇₁BM** (Figure 2d–f and

Figure S4, Supporting Information). The 2D scattering patterns were collected on a Pilatus 1M-F pixel detector, and the in-plane scattering profiles versus q were obtained by integrating the data from the patterns (Figure 2f) near the specular beam position ($q_z = 0.032 \text{ \AA}^{-1}$) for best intensity. In order to assigning the scattering peaks in GISAXS in the in-plane direction q_y (scattering wavevector component in the in-plane direction), a series of as-cast and post-treated **DRCN5T:PC₇₁BM** samples with different weight ratios varying from 1:0, 1:0.3, 1:0.5, to 1:0.8 were measured under the same conditions.^[61] As shown in Figure S4 (Supporting Information), the scattering peak is gradually enhanced with increasing the content of **PC₇₁BM**. Thus the broad peaks in the in-plane direction at q_y of ≈ 0.012 and 0.014 \AA^{-1} (Figure 2f) in the as-cast and post-treated **DRCN5T:PC₇₁BM** blend respectively are ascribed to the scattering of increasingly ordered and enhanced fullerene aggregates with increased mean spacing.^[62,63] The relatively enhanced shoulder peak for the post-treated film corresponds to stronger phase separation of fullerenes with larger aggregated **PC₇₁BM** domains. These GISAXS features are largely consistent with the results from DF-STEM (Figure 1e,f). Using an ellipsoidal model (with major and minor axes of $2A$ and $2B$), together with a hard-sphere structure factor form factor for the **PC₇₁BM** aggregates,^[62,63] we have fitted the GISAXS profiles reasonably well (Figure 2f and Figure S4, Supporting Information). Data in the very low- q region of the profiles with a sharper increase in intensity are accounted for mainly by using the Debye–Bueche correlation function with a correlation length ξ for very large clusters of **PC₇₁BM**. The fitted parameters are summarized in Table 1, the ellipsoid **PC₇₁BM** aggregates with $2A = 8.5 \text{ nm}$ and $2B = 30.9 \text{ nm}$ in the as-cast film grow substantially to $2A = 11.4$ and $2B = 34.2 \text{ nm}$ after post-treatment. Correspondingly, the mean aggregate distance L is enlarged from

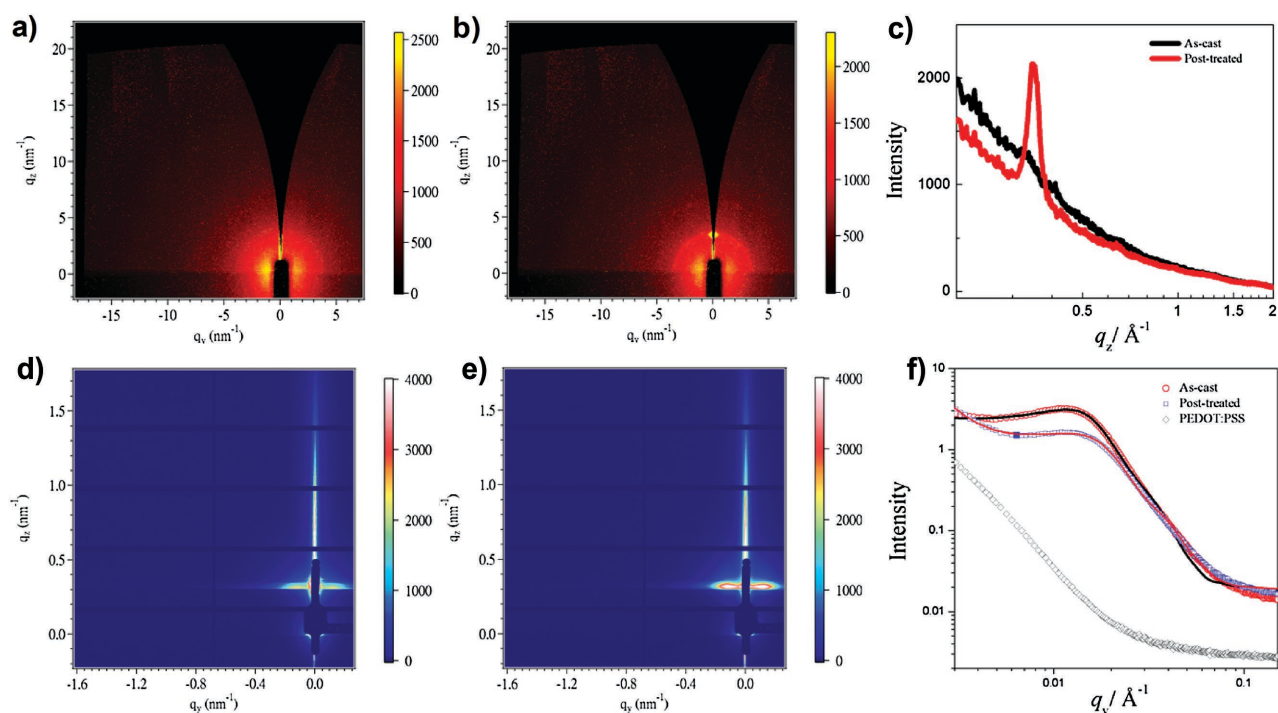


Figure 2. The GIWAXS patterns of the as-cast a) and post-treated b) **DRCN5T:PC₇₁BM** blend films. c) The corresponding out-of-plane GIWAXS profiles of the as-cast and post-treated **DRCN5T:PC₇₁BM** blend films. d,e) The GISAXS patterns of the as-cast d) and post-treated e) **DRCN5T:PC₇₁BM** blend films. f) The corresponding in-plane GISAXS profiles and fittings (solid curves) of the as-cast and post-treated **DRCN5T:PC₇₁BM** blend films. The very different GISAXS profile of a similar PEDOT:PSS layer on Si profile used for all samples is also shown for comparison.

37.8 to 41.7 nm (as estimated from the fitted volume fraction of the aggregates). Based on the above morphology analysis from GIWAXS and GISAXS, it is convincing that highly crystalline fibrillar-type donor domains mutually dispersed with fullerene aggregate domains are formed after post-treatment, which could enhance the p-type and n-type domain connectivity and improve both hole and electron-transport ability across the film toward efficiently charge extractions.

2.3. The Number of Absorbed Photons in Two Different Morphologies

The two different morphologies will significantly influence their UV–vis absorption spectra, and thus the number of absorbed photons in the active layers. As shown in **Figure 3a**, the absorption maxima of as-cast **DRCN5T:PC₇₁BM** (551 nm) blend with amorphous morphology exhibits a very

Table 1. Fitted structural parameters from the in-plane GISAXS profiles for the ellipsoidal aggregates in the as-cast and post-treated films of **DRCN5T:PC₇₁BM**, including the major and minor axes $2A$ and $2B$, the mean aggregate distance L deduced from the fitted volume fraction, and the Debye–Bueche correlation length ξ .

DRCN5T:PC ₇₁ BM	2A [nm]	2B [nm]	L [nm]	ξ [nm]
As-cast	8.5 ± 0.1	30.9 ± 0.2	37.8	67.2
Post-treated	11.4 ± 0.1	34.2 ± 0.2	41.7	59.2

large blueshift (131 nm) compared to its pristine **DRCN5T** film. It is even closer to the absorption maxima of **DRCN5T** in chloroform (531 nm),^[27] while the post-treated blend film gives a significantly enhanced absorption coefficient with the strong shoulder peak at 678 nm. This is attributed to the completely disrupt of the crystallized **DRCN5T** domains by aggregated PC₇₁BM clusters in the as-cast state as discussed above. Meanwhile, the crystallinity of neat **DRCN5T** film is significantly enhanced after post-treatment, which is evident from the formation of the vibronic shoulder peak. This peak is reproduced after further post-treatment of the blended film with PC₇₁BM. Then the absorption spectra of single **DRCN5T** molecule and **DRCN5T- π -dimer** were modeled based on theoretical calculations (**Figure S5**, Supporting Information), and consistent results with the experimental UV–vis absorption spectra was obtained. From single molecule to the anti-para π – π stacking dimer, the simulated absorption spectrum exhibits a very large redshift, which further confirms the importance of donor packing (morphology) in the active layer on their respected absorption properties. For the simulated absorption of the **DRCN5T- π -dimer**, the oscillator strength at 607.63 nm (**Table S2**, Supporting Information) should account for the contribution from intermolecular charge transfer, which is consistent with the observation of shoulder peak in the post-treated blend film. The interpretation also concurs with the findings from the photoluminescence (PL) spectra, where the PL intensity for the pure **DRCN5T** film after post-treatment is significantly enhanced since the nonradiative recombination through the interfacial traps and disorder are much reduced, while that

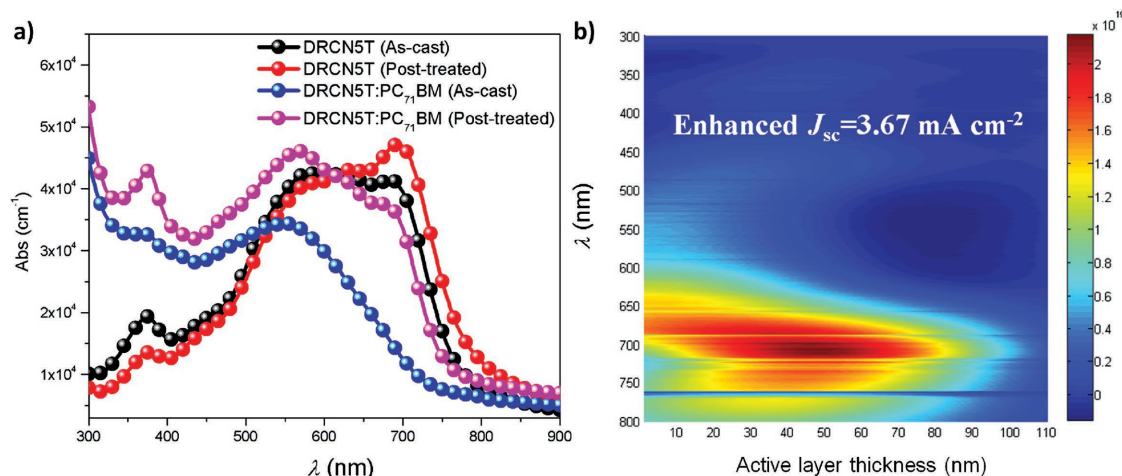


Figure 3. a) UV-vis absorption spectra of the neat **DRCN5T** films and the **DRCN5T:PC₇₁BM** films before and after post-treatment. b) The enhanced number of absorbed photons in the **DRCN5T:PC₇₁BM** blends after post-treatment as a function of depth of the active layer calculated using a 1D transfer matrix model. The incident light entered the device from the left of the figure (0 nm at the *x*-axis).

for the as-cast blend film (with PC₇₁BM) is much more efficiently quenched (Figure S6, Supporting Information).

The total number of absorbed photons in the real devices could be significantly influenced by redistributing the electric field due to the two different morphologies. The exciton generation rates were calculated by spatially integrating the absorbed photon flux density within the active layer from the distribution of incident light intensity ($|E|^2$) inside the devices using the transfer matrix model (TMM) approach (Figure S7, Supporting Information).^[64] As shown in Figure 3b, the enhanced generation of excitons after the post-treatment were mainly located from 600 to 800 nm, which is consistent with the enhanced vibronic shoulder peak in the UV-vis absorption spectra (Figure 3a). Thus the simulated short-circuit current density ($J_{sc, \text{simu}}$, assuming the internal quantum efficiency reached 100%) increases significantly from 14.13 to 17.80 mA cm⁻² for the as-cast and post-treated **DRCN5T:PC₇₁BM** devices under the optimized processing conditions, respectively.

Next, to discern the influence of two different morphologies on the charge generation and extraction dynamics, transient absorption studies over the femtosecond to microsecond time-scales were performed.

2.4. Charge Generation Dynamics of Two Different Morphologies

Before probing the charge carrier dynamics of the **DRCN5T:PC₇₁BM** blends, the TA profiles and dynamics of the pristine **DRCN5T** films with or without post-treatment were first investigated and presented in Figure S8 (Supporting Information). In brief, the neat **DRCN5T** film shows positive differential transmittance ($\Delta T/T$) signals below ≈ 770 nm with a sharp peak at ≈ 710 nm corresponding to the ground-state-bleaching (GSB) of the **DRCN5T** molecule due to the state-filling of the excited states. The broad and negative $\Delta T/T$ transient signals were observed in the near-infrared (NIR) region with a peak centered at ≈ 1200 nm being attributed to the dominating

photoinduced absorption (PIA) of **DRCN5T** singlet EX. The TA profiles and exciton dynamics for the post-treated **DRCN5T** film are very similar with that of the pristine films without post-treatment. This indicates that both as-cast and post-treated **DRCN5T** films exhibit very good crystallinity, which is consistent with the vibronic peaks signature shown in Figure 3a. However, the differences are striking when **DRCN5T** is blended with PC₇₁BM. **Figure 4** shows the transient absorption profile spanning from 520 to 1500 nm at varying delay times following photoexcitation with 500 nm pulses, and the magnitude of $\Delta T/T$ was corrected by the absorption difference of **DRCN5T:PC₇₁BM** blends without and with post-treatment. The as-cast **DRCN5T:PC₇₁BM** film shows a featureless GSB profile and the absence of the sharp GSB peak at ≈ 710 nm, indicating a disruption of the **DRCN5T** organization by the presence of PC₇₁BM. Hence the blend is predominantly by amorphous phase. With post-treatment, the morphology disruption by PC₇₁BM is significantly alleviated (see also Figure S9, Supporting Information for the zoom-in GSB profiles). The presence of the prominent sharp peak at 710 nm and the vibronic peaks reemerge, exhibiting the GSB profile resembles to that of the pristine **DRCN5T** film. The redshift and the appearance of vibronic shoulders in the GSB profile of the post-treated film are analogous to that of poly[3-hexylthiophene-2,5-diyl] (P3HT):PC₆₁BM ([6,6]-phenyl-C₆₁-butyric acid methyl ester) after thermal annealing, which indicates the presence of well-ordered regions in the post-treated **DRCN5T:PC₇₁BM** film with strong interchain interaction as well as exciton-phonon coupling.^[54,65]

In the NIR region, the signature of exciton PIA in the as-cast **DRCN5T:PC₇₁BM** film is slightly blueshifted to around ≈ 1150 nm compared with that in pure **DRCN5T** and post-treated **DRCN5T:PC₇₁BM** film. Additionally, the initial EX signal is much stronger in the post-treated **DRCN5T:PC₇₁BM** film than that in the as-cast film, indicating that a large fraction of excitons in the post-treated **DRCN5T:PC₇₁BM** film are not immediately split due to the formation of large crystalline domains. These excitons need to diffuse over a longer distance through the crystalline domains to reach at the interface where they

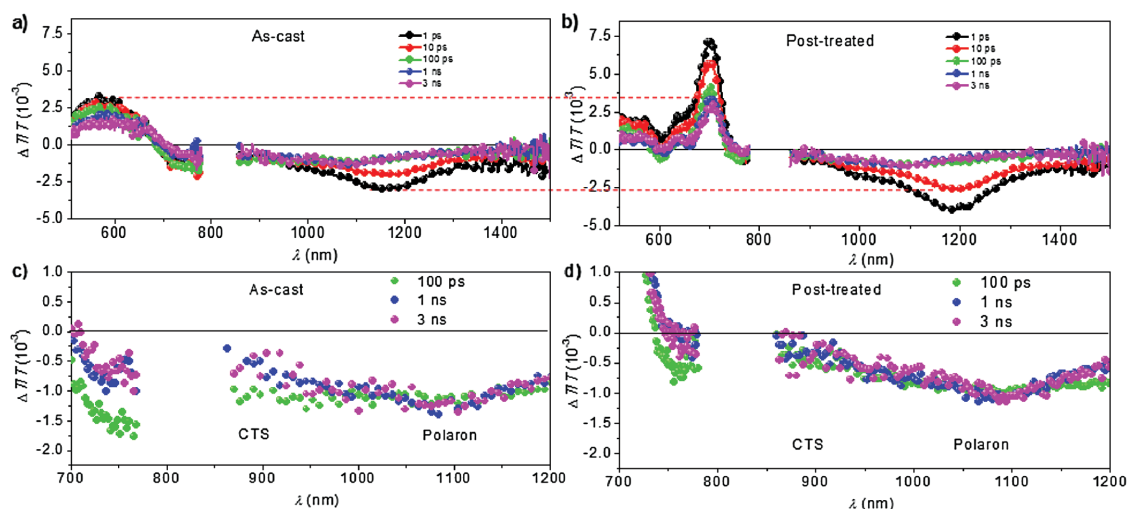


Figure 4. The fs-ns transient absorption profiles at selected delay times for the as-cast a) and post-treated b) **DRCN5T:PC₇₁BM** blend films. The zoom-in TA profile between 700 and 1200 nm region shows the evolution of CTSs and polaron bands in the as-cast c) and post-treated d) **DRCN5T:PC₇₁BM** blend films.

are subsequently quenched by PC₇₁BM. After the decay of the EX signal at ≈ 100 ps delay, a long-lived PIA peak centered at ≈ 1100 nm becomes prominent. This long-lived component, which exists up to a few microseconds (shown later) is attributed to the polaron-induced absorption. By comparing the magnitude of the polaron PIA at ≈ 3 ns (Figure 4c,d), we infer that the initial generation of free charges after 500 nm laser excitation for the post-treated film is as efficient as that in the as-cast film. This indicates the exciton diffusion length in the post-treated film is larger than the fibrillar domain size and they can be efficiently split at the interfaces. To investigate the polaron generation mechanisms, we extracted the dynamics at 1100 nm and fitted them with multiexponential function (Figure 5a). Apart from the lifetimes of <5 and <100 ps, which are attributed to EX for the PIA at 1100 nm (Table 2), we found a long-lived component (that extends beyond the measurement window) with a very slow rising constant of 1020 ± 90 ps and 920 ± 80 ps for the as-cast and post-treated films, respectively. Meanwhile, the PIA at around 750–950 nm region relaxes with a time

constant of about 1000 ps that corresponds to the slow rise of polaron signals, and thus we attribute this lifetime to the decay of the CTSs (Figures 4c,d and 5b).^[52,66] This assignment is also consistent with the reported spectra position of the PIA band due to CTSs for polymer-based OPVs.^[56,66,67] The rising of the CTS absorption is almost instantaneously (<1 ps) after photoexcitation for the as-cast film, indicating the fast or direct formation of the CTS at the amorphous donor:acceptor interface after excitation. For the post-treated film, however, we have observed both an instantaneous (<1 ps) and a slow (≈ 20 ps) formation of the CTS, each of which contributes $\approx 50\%$ to the final signal (Figure S10, Supporting Information). This is consistent with the migration of excitons from the crystalline domain center to the donor:acceptor interface where CTSs are formed. In addition, the CTSs for the post-treated film exhibit much weaker PIA signals than that of the as-cast film, which indicates that the CTSs were almost totally suppressed after post-treatment.

Then the exciton diffusion efficiencies in both morphologies were calculated according to Equation (1)^[51]

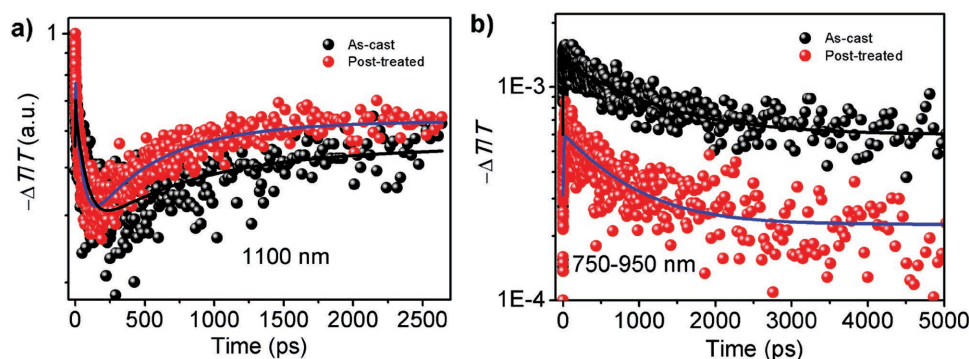


Figure 5. a) The fs-ns transient dynamics for the as-cast and post-treated **DRCN5T:PC₇₁BM** films monitored at 1100 nm. b) The fs-ns transient dynamics for the as-cast and post-treated **DRCN5T:PC₇₁BM** films monitored at 750–950 nm regions. The solid lines represent the multiexponential fitting of these dynamics.

Table 2. Summary of the decay constants extracted from the multi-exponential fitting of the dynamics for the as-cast and post-treated DRCN5T:PC₇₁BM films. The long-lived component in the 1100 nm PIA extends beyond our measurement window, which is simply fitted with an arbitrary long lifetime and termed as “Long.”

DRCN5T:PC ₇₁ BM	λ [nm]	τ_1 [ps]	τ_2 [ps]	τ_3 [ps]
As-cast	1100	3.2 ± 0.5 (22%)	99 ± 6 (33%)	Long (45%) Rise time: 1017 ± 91
	750–950	1040 ± 40 (65%)	Long (35%)	–
Post-treated	1100	4.4 ± 0.7 (21%)	50 ± 5 (31%)	Long (48%) Rise time: 918 ± 76
	750–950	900 ± 80 (55%)	Long (45%)	–

$$\eta_{ED} = \frac{k_q}{(k_p + k_q)} \quad (1)$$

where k_q is the dissociation rate of singlet exciton in blend film, k_p is the deactivation rate of singlet excitons in pristine DRCN5T films (Table S4, Supporting Information). In the as-cast film, the η_{ED} is estimated to be as high as 99%, which is almost the same with that after post-treatment (98%). Since the fullerene clusters are well dispersed in the amorphous donor matrix in the as-casted DRCN5T:PC₇₁BM blend, there exist enough interfacial surface area and no exciton diffusion is needed, and this is the reason for the very efficient “exciton diffusion efficiency” of 99% in the as-casted blends. On the other hand, this further confirms that crystallized fibrillar morphology with bicontinuous network could also have very efficient exciton diffusion.

The presence of high density of CTSs but lower yield of polarons in the as-cast films implies a heavier loss of CTSs through geminate recombination. To quantify the loss through geminate recombination, one could estimate how much initial photoexcitation relaxes to ground state through the dynamics of the GSB. As shown in Figure S11 (Supporting Information), we have fitted the GSB dynamics within 5 ns that comprises of EX, CTSs, and polaron signal. It is found that the ratio between CTSs and polaron is 1:2.1 for the as-cast film and 1:4.5 for the post-treated film, respectively. This verifies that the exciton dissociation efficiency (η_{CD}) for the as-cast film is only 68%, which increases significantly to 82% after post-treatment.

2.5. Charge Recombination and Extraction Dynamics of Two Different Morphologies

To investigate the effects of morphology on the charge recombination dynamics, we have also performed TA measurements over the nanosecond-microsecond (ns- μ s) time regime. Figure 6a–c shows the ns- μ s TA profiles at selected time delays (1, 10, and 100 ns) for these blend films. The as-cast film shows a much higher magnitude of CTSs signals (870–950 nm) than the post-treated film. This indicates that the charge carriers in the as-cast film prefer to form CTSs than that in the post-treated film. A large proportion of charge carriers in the as-cast film are strongly bounded charge pairs rather than spatially free

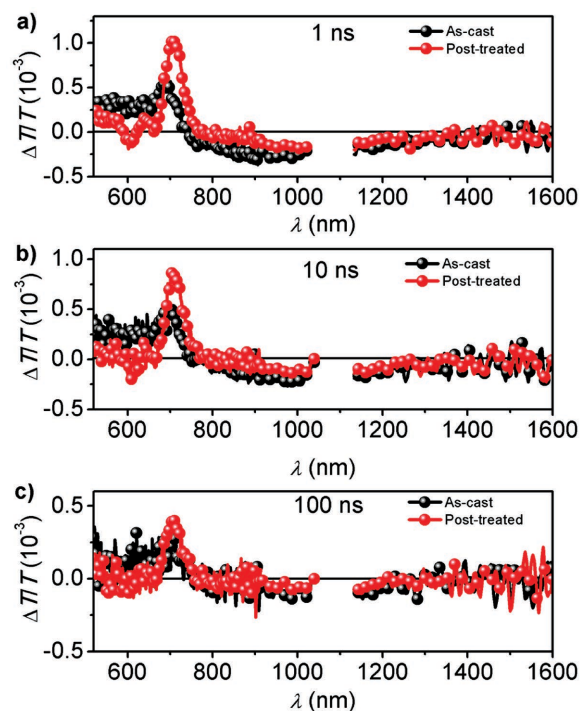


Figure 6. The ns- μ s transient profiles for the as-cast and post-treated DRCN5T:PC₇₁BM films monitored at 1 ns a), 10 ns b), and 100 ns c) delay.

charges, and these bounded charge pairs can be easily recombined via the CTSs.

The dynamics of CTSs (averaging over 870–950 nm) for both films are shown in Figure 7a,b. Both CTSs show weak intensity-dependence decay, indicating that the charges located in CTSs are bound charge pairs, which mainly undergo rapid geminate recombination. In addition, the CTSs can also act as interfacial traps for Shockley–Read–Hall type trap-assisted recombination which is also a monomolecular process.^[68–70] The polaron band (averaging between 1150 and 1250 nm) has a longer lifetime than the CTSs band (Figure 7c,d). Importantly, the charge recombination in the polaron band displays strong intensity dependence, which indicates this recombination is Langevin type trap-free bimolecular recombination. A modified bimolecular recombination formula is employed to fit these dynamics (Figure S12, Supporting Information)

$$\frac{dN}{dt} = -\gamma N^\alpha N^2 \quad (2)$$

where N is the free carrier density, γ is the prefactor of bimolecular recombination, and α accounts for concentration dependent carrier mobility in organic materials.^[52,53] The fitting results are listed in Table S5 (Supporting Information). The effective Langevin coefficient defined by

$$\gamma_{\text{eff}} = \gamma N^\alpha \quad (3)$$

for the post-treated films reaches $7.2 \times 10^{-12} \text{ cm}^3 \text{ s}^{-1}$, which is faster compared to that of the as-cast film ($5.4 \times 10^{-12} \text{ cm}^3 \text{ s}^{-1}$). The increase can be attributed to the much higher carrier

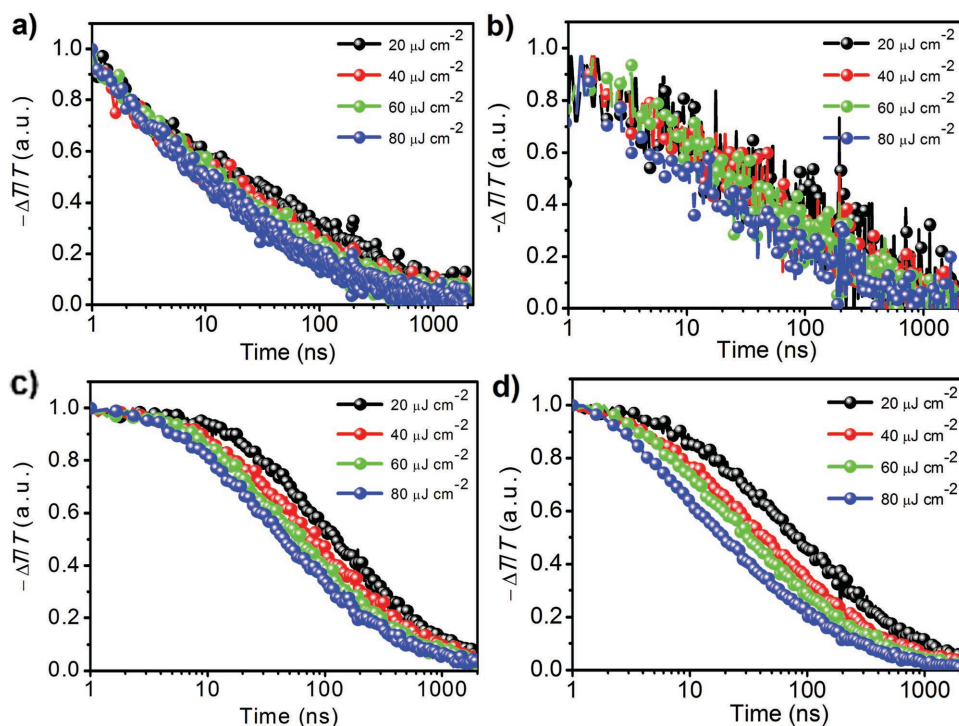


Figure 7. Intensity-dependent CTSs dynamics for the as-cast a) and post-treated b) **DRCN5T:PC₇₁BM** film monitored at 870–950 nm. Intensity-dependent polaron dynamics for the as-cast c) and post-treated d) **DRCN5T:PC₇₁BM** film monitored at 1150–1250 nm regions.

mobilities in the post-treated films. Correspondingly, the hole and electron mobilities in both as-cast and post-treated films were measured by space-charge limited current (SCLC) method. The hole mobility is dramatically improved from 1.05×10^{-4} to $6.54 \times 10^{-4} \text{ cm}^2 \text{ V}^{-1} \text{ s}^{-1}$ after post-treatment, while the electron mobility also increases significantly from 2.88×10^{-5} to $2.53 \times 10^{-4} \text{ cm}^2 \text{ V}^{-1} \text{ s}^{-1}$. Next, the charge carrier diffusion lengths in these two films can be estimated through Equation (4) (only considering the 1D transport)

$$L_D = \sqrt{\mu V_T \tau} \quad (4)$$

where μ is the carrier mobility, V_T is the thermal energy, and τ is the carrier lifetime. τ can be estimated by using

$$\frac{dN}{dt} = -\gamma_{\text{eff}} N^2 = -\frac{1}{\tau} N \quad (5)$$

which is a concentration-dependent parameter. Under 1 sun condition, the effective charge carrier lifetimes for the as-cast and post-treated devices under open-circuit conditions are around 5 and 3 μs , respectively. This yields the electron and hole diffusion lengths of 19.0 and 36.2 nm in the as-cast devices, respectively. The diffusion lengths in the post-treated devices significantly improve to 43.6 and 70.0 nm for electrons and holes (the half thickness of the active layer is 55 nm), respectively. Under short-circuit conditions, the diffusion lengths could be even longer owing to the much reduced charge carrier concentration. The longer charge diffusion length in the post-treated device is consistent with the improved percolation

and high efficiency in extracting the photogenerated charges after post-treatment.

Based on the above fs- μs transient absorption studies, we speculate that the presence of higher density of CTSs and the heavy loss by geminate recombination and nongeminate recombination are the causes of the low FF and field-dependent J - V characteristics under operation conditions for the as-cast devices. The further post-treatment could generate the crystallized fibrillar network, which provides the effective percolated pathways for both holes and electrons transport to the electrodes. Such benign structure with decreased interfacial CTSs can reduce the geminate losses as well as the trap-assisted nongeminate losses. This is also consistent with the light-intensity-dependent current-voltage experiments and photocurrent density-effective voltage analyses shown in Figures S13–S15 (Supporting Information).^[71,72]

Now, the remaining question is to evaluate the influence of two different morphologies on the charge transport and collection efficiency. In order to quantitatively compare them, Equation (6)^[51] is used to calculate these efficiencies

$$\eta_{\text{CC}} = \eta_{\text{EQE}} / \eta_{\text{A}} / \eta_{\text{ED}} / \eta_{\text{CD}} \quad (6)$$

where η_{CC} is the charge collection efficiency, η_{EQE} is the external quantum efficiency (EQE), η_{A} is the absorption efficiency, η_{ED} is the exciton diffusion efficiency, and η_{CD} is the exciton dissociation efficiency.

As shown in Table 3, the charge collection efficiency at 500 nm excitation is close to 100% in the post-treated **DRCN5T:PC₇₁BM** device, while it is only 81% in the as-cast

Table 3. Summary of the efficiency of each fundamental photovoltaic conversion processes in **DRCN5T:PC₇₁BM**-based solar cells with two different morphologies.

	η_A [%] ^{a)}	η_{ED} [%]	η_{CD} [%]	η_{CC} [%]	EQE [%] ^{b)}
As-cast	82	99	68	81	44
Post-treated	85	98	82	100	68

^{a)}The absorption efficiency at 500 nm from optical simulation (Figure S7, Supporting Information); ^{b)}The EQE at 500 nm (Figure S16, Supporting Information).

device. This is also consistent with the longer hole and electron diffusion lengths as discussed above. Therefore, we conclude that the amorphous morphology in the lack of percolated pathways would generate large amount of strongly bounded charge transfer states. These strongly bounded CTs could only be dissociated and extracted by applying very large reverse voltages,^[24,57–59] thus contributes to the electric field dependent J - V characteristics (lower FF) and poorer OPV device performances (Figures S1 and S12, Supporting Information). The in-depth work to distinguish the electric field dependent exciton dissociation and charge extraction, and their relationship with morphologies and device performances is now carrying out.

3. Conclusions

Using one of the best performing bulk-heterojunction type SM-OPV system-**DRCN5T:PC₇₁BM** as a model, we have systematically investigated the origins of the electric field dependent/independent J - V behaviors by discerning the complex interplay between the active layer morphology and excited state dynamics, and correlating with the device performance. The amorphous morphology in the lack of percolated pathways promotes the formation of the strongly bounded CTs, which predominantly undergo the geminate recombination or function as interfacial traps that facilitate the nongeminate recombination of charge carriers. These strongly bounded CTs could only be dissociated and extracted by applying very large reverse voltages, thus giving rise to the electric field dependent J - V characteristics. On the other hand, these CTs are almost completely diminished owing to the formation of the bicontinuous network with crystallized fibrillar morphology after post-treatment, which acts as “highways” for the effective exciton diffusion to the interfaces and subsequent dissociation. Then the separated charges are transported and extracted by the built-in potential with almost 100% efficiency, which is consistent with the longer and ambipolar diffusion lengths found in the post-treated system. The ratio between the CTs and polaron populations are 1:2.1 and 1:4.5 for the as-cast and post-treated films, respectively, which demonstrates the exciton dissociation efficiency increases significantly from $\approx 68\%$ for the as-cast film to $\approx 82\%$ after post-treatment. The results gained in this work provide new insights to investigate the origin of different J - V behaviors for bulk-heterojunction organic solar cells from morphology aspects and excited state dynamics, which could be directly employed to guide the further optimization of the performance of SM-OPVs through judicious morphology control and engineering.

4. Experimental Section

Materials Preparation: All reactions and manipulations were carried out under an argon atmosphere using standard Schlenk techniques. PC₇₁BM was purchased from American Dye Source, Inc. **DRCN5T** was synthesized using our previously reported method.^[27]

Device Fabrication and Characterization: The conventional devices were fabricated with the structure: glass/Indium Tin oxide (ITO)/poly[3,4-ethylenedioxythiophene]:poly[styrenesulfonate] (PEDOT:PSS)/**DRCN5T:PC₇₁BM**/poly[(9,9-bis(3′-(N,N-dimethylamino)propyl)-2,7-fluorene)-alt-2,7-(9,9-dioctylfluorene)] (PFN)/Al. The ITO-coated glass substrates were cleaned by ultrasonic treatment in detergent, deionized water (DI), acetone, and isopropyl alcohol for 15 min each and subsequently dried by blowing nitrogen. A thin layer of PEDOT:PSS (Baytron P VP Al 4083, filtered at 0.45 μm) was spin coated (3000 rpm, ≈ 40 nm thick) onto an ITO surface. After being baked at 150 °C for 20 min, the substrates were transferred into an argon-filled glove box. Subsequently, the active layer was spin casted from blend ratios (w/w, 1:0.8) of **DRCN5T** (10 mg mL⁻¹) and PC₇₁BM in a chloroform solution at 1700 rpm for 20 s on the ITO/PEDOT:PSS substrate. Then thermal annealing was performed at 120 °C for 10 min, and solvent vapor annealing in chloroform environment for 60 s. Finally, a thin layer of PFN from its methanol solution was spin coated onto the active layer and 60 nm Al layer was deposited on the active layer under high vacuum ($<1.5 \times 10^{-4}$ Pa).

The effective area of each cell was about 4 mm² defined by masks. The thickness of the active layer (≈ 110 nm) was measured using a Dektak 150 profilometer. Atomic force microscope (AFM) investigation was performed using Bruker MultiMode 8 in “tapping” mode.

The current density–voltage (J - V) curves of the photovoltaic devices were obtained by using a Keithley 2400 source-measure unit. The photocurrent was measured under illumination simulated 100 mW cm⁻² (AM 1.5G) irradiation using a xenon-lamp-based solar simulator [Oriel 96000 (AM 1.5G)] in an argon-filled glove box. The irradiance was calibrated using a certified silicon diode.

EQE values of the encapsulated devices were measured using a lock-in amplifier (SR810, Stanford Research Systems). The devices were illuminated by monochromatic light from a 150 W xenon lamp passing through an optical chopper and a monochromator. Photon flux was determined by a calibrated standard silicon photodiode.

Mobility measurements of **DRCN5T/PC₇₁BM** (w/w, 1:0.8) blend films with and without post-treatment were carried out with the following diode structures: ITO/PEDOT:PSS/active layer/Au for hole and Al/active layer/Al for electron by taking current–voltage curve in the range of 0–7 V. The charge carrier mobilities were calculated using the SCLC^[73] model

$$J = \frac{9\epsilon_0\epsilon_r\mu_0V^2}{8L^3} \exp\left(0.89\beta\sqrt{\frac{V}{L}}\right) \quad (7)$$

where J is the current density, L is the film thickness of the active layer, μ_h is the hole mobility, ϵ_r is the relative dielectric constant of the transport medium, ϵ_0 is the permittivity of free space (8.85×10^{-12} F m⁻¹), V ($= V_{\text{appl}} - V_{\text{bi}}$) is the internal voltage in the device, where V_{appl} is the applied voltage to the device and V_{bi} is the built-in voltage due to the relative work function difference of the two electrodes.

Theoretical Calculation: The molecular structures the single **DRCN5T** molecule and anti-para π - π stacking dimer were optimized by density functional theory calculations at the level of wB97XD/6-31G*,^[74] and the frequency analysis was followed to assure that the optimized structures were stable states. To simplify the calculations, the octyl groups in the oligothiophene donors were replaced by simpler ethyl groups. The $S_0 \rightarrow S_n$ transitions were calculated by using Zerner’s intermediate neglect of differential overlap (ZINDO) level of theory based on the optimized structures. All theoretical calculations were carried out by using the Gaussian 09 package.^[75]

Optical Simulations: The optical simulation was modeled using a TMM, the matrix laboratory (MATLAB) program is available online at <http://mcgeheegroup.stanford.edu/transfermatrix>. The 1D spatial distribution of normalized incident light intensity ($|E|^2$) inside the devices was calculated by means of an optical TMM approach. The spatial

distribution of the absorbed photon flux density could then be calculated by integrating single-wavelength $|E|^2$ with an AM 1.5G spectrum from 300 to 800 nm. Finally, the theoretical maximum J_{sc} for a device under AM 1.5G illumination was determined by spatially integrating the absorbed photon flux density within the active layer, assuming 100% internal quantum efficiency for all wavelengths.

Light Intensity Experiment: In order to investigate the dependence of J_{sc} on the light intensity, the intensity of the light was modulated with a series of two neutral density filters wheels of six filters apiece, allowing for up to 17 steps to adjust the intensity from 100 to 5 mW cm⁻².

TEM and STEM: The active layers were immersed in DI water for exfoliation and then transferred to a Cu foil for image recording. The TEM and STEM (FEI Talos F200X TEM) was operated at 200 keV, with gun lens of 3.6 and TEM spot size of 9. TEM bright-field images were obtained by FEI Talos F200X TEM, which equipped with the beam-blank function.

GIWAXS/GISAXS: For GIWAXS/GISAXS measurements, the active layers were spin casted on silicon wafers with pre-coated PEDOT:PSS, and then were selectively subject to the similar post-treatment as that for the device film. GIWAXS/GISAXS measurements were performed at the 23A Small and Wide Angle X-ray Scattering (SWAXS) Endstation of the National Synchrotron Radiation Research Center (NSRRC) in Taiwan, using a complementary metal oxide semiconductor (CMOS) flat-panel C10158DK-3957(X) area detector for GIWAXS and a Pilatus 1M-F area detector for GISAXS.^[76] With the sample surface defined in the x-y plane and the incident X-rays in the x-z plane, the scattering wavevector transfer $q = (q_x, q_y, q_z)$ can be decomposed into three orthogonal components of $q_x = 2\pi\lambda^{-1}(\cos\beta\cos\phi - \cos\alpha)$, $q_y = 2\pi\lambda^{-1}(\cos\beta\sin\phi)$, and $q_z = 2\pi\lambda^{-1}(\sin\alpha + \sin\beta)$, where α and β stand for the incident and exit angles and ϕ for the scattering angle away from the y-z plane; λ is the wavelength of the X-rays. The 10 keV X-ray beam of 0.2 mm diameter was used with a sample incident angle 0.2°; the sample-to-detector distances were 5.0 m (covering the q -region 0.003–0.16 Å⁻¹) and 26 cm for GIWAXS (0.2–2.5 Å⁻¹). All the GISAXS data presented were subtracted with the scattering from a similar PEDOT:PSS film on Si wafer measured under the same conditions.

Transient Absorption Spectroscopy: Transient absorption measurements were performed using commercial Helios and EOS setups (Ultrafast Systems LLC). The films were measured under an inert atmosphere to avoid oxidation and degradation. The transient dynamics in the fs–ns time region (50 fs–5 ns) were acquired by Helios, which works in a nondegenerate pump–probe configuration. The pump pulses (500 nm) were generated from an optical parametric amplifier (Coherent OPerA Solo) that was pumped by a 1 kHz regenerative amplifier (Coherent Libra, 800 nm, 50 fs, 4 mJ). A mode-lock Ti-sapphire oscillator (Coherent Vitesse, 80 MHz) was used for the seeding. The probe pulses were a white light continuum generated by passing the 800 nm fs pulses through either a 2 mm sapphire plate for visible part (400–800 nm) or a 1 cm sapphire plate for NIR part (800–1600 nm). The transient dynamics in the ns– μ s region (1 ns–5 μ s) were acquired by EOS. The pump beam was the same with that used in Helios. The probe beam EOS was a white continuum generated from a photonic fiber using a Neodymium doped Yttrium Aluminum Garnet (Nd:YAG) laser (1064 nm). The probe light was collected using a CMOS sensor for UV–vis part and InGaAs diode array sensor for NIR part. To reduce the noise due to laser fluctuations, another similar sensor was used to collect the probe light before the sample to be used as a reference.

Supporting Information

Supporting Information is available from the Wiley Online Library or from the author.

Acknowledgements

G.L. and B.W. contributed equally to this work. The authors gratefully acknowledge financial support from the Ministry of Science and

Technology of China (Grant Nos. 2014CB643502 and 2012CB933401), National Natural Science Foundation of China (Grant Nos. 91433101, 51422304, 51373078, and 11304354), Natural Science Foundation of Tianjin City (Grant No. 13RCFGX01121), and Program for Changjiang Scholars and Innovative Research Team (IRT1257) the NTU start-up grant M4080514, SPMS collaborative Research Award M4080536, Ministry of Education (MOE) Tier 1 grant RG101/15, and MOE AcRF Tier 2 grants MOE2013-T2-1-081 and MOE2014-T2-1-044; and from the Singapore National Research Foundation through the Singapore-Berkeley Research Initiative for Sustainable Energy (SinBeRISE) CREATE Programme. The authors thank Prof. Andong Xia and Xian Wang for the absolute PL quantum yield measurement, and the FEI company for providing the TEM and STEM measurements and the beamline BL16B1 (Shanghai Synchrotron Radiation Facility) for providing beam time.

Received: May 9, 2016

Revised: June 25, 2016

Published online:

- [1] P. M. Beaujuge, J. M. J. Fréchet, *J. Am. Chem. Soc.* **2011**, *133*, 20009.
- [2] Y. Li, *Acc. Chem. Res.* **2012**, *45*, 723.
- [3] Y. Liang, L. Yu, *Acc. Chem. Res.* **2010**, *43*, 1227.
- [4] H. Zhou, L. Yang, W. You, *Macromolecules* **2012**, *45*, 607.
- [5] L. Ye, S. Zhang, L. Huo, M. Zhang, J. Hou, *Acc. Chem. Res.* **2014**, *47*, 1595.
- [6] S. H. Liao, H. J. Jhuo, Y. S. Cheng, S. A. Chen, *Adv. Mater.* **2013**, *25*, 4766.
- [7] P. L. Boudreault, A. Najari, M. Leclerc, *Chem. Mater.* **2011**, *23*, 456.
- [8] Z. He, B. Xiao, F. Liu, H. Wu, Y. Yang, S. Xiao, C. Wang, T. P. Russell, Y. Cao, *Nat. Photonics* **2015**, *9*, 174.
- [9] G. Li, V. Shrotriya, J. S. Huang, Y. Yao, T. Moriarty, K. Emery, Y. Yang, *Nat. Mater.* **2005**, *4*, 864.
- [10] Y. Zhao, Z. Xie, Y. Qu, Y. Geng, L. Wang, *Appl. Phys. Lett.* **2007**, *90*, 043504.
- [11] W. Ma, C. Yang, X. Gong, K. Lee, A. J. Heeger, *Adv. Funct. Mater.* **2005**, *15*, 1617.
- [12] J. Peet, J. Y. Kim, N. E. Coates, W. L. Ma, D. Moses, A. J. Heeger, G. C. Bazan, *Nat. Mater.* **2007**, *6*, 497.
- [13] V. Vohra, K. Kawashima, T. Kakara, T. Koganezawa, I. Osaka, K. Takimiya, H. Murata, *Nat. Photonics* **2015**, *9*, 403.
- [14] Y. Liu, J. Zhao, Z. Li, C. Mu, W. Ma, H. Hu, K. Jiang, H. Lin, H. Ade, H. Yan, *Nat. Commun.* **2014**, *5*, 5293.
- [15] J. You, L. Dou, K. Yoshimura, T. Kato, K. Ohya, T. Moriarty, K. Emery, C. C. Chen, J. Gao, G. Li, Y. Yang, *Nat. Commun.* **2013**, *4*, 1446.
- [16] S. Zhang, L. Ye, W. Zhao, B. Yang, Q. Wang, J. Hou, *Sci. China: Chem.* **2015**, *58*, 248.
- [17] J. Huang, C.-Z. Li, C.-C. Chueh, S.-Q. Liu, J.-S. Yu, A. K. Y. Jen, *Adv. Energy Mater.* **2015**, *5*, 201500406.
- [18] B. Walker, C. Kim, T. Q. Nguyen, *Chem. Mater.* **2011**, *23*, 470.
- [19] A. Mishra, P. Bäuerle, *Angew. Chem., Int. Ed.* **2012**, *51*, 2020.
- [20] Y. Lin, Y. Li, X. Zhan, *Chem. Soc. Rev.* **2012**, *41*, 4245.
- [21] J. E. Coughlin, Z. B. Henson, G. C. Welch, G. C. Bazan, *Acc. Chem. Res.* **2013**, *47*, 257.
- [22] Y. Chen, X. Wan, G. Long, *Acc. Chem. Res.* **2013**, *46*, 2645.
- [23] J. Roncali, P. Leriche, P. Blanchard, *Adv. Mater.* **2014**, *26*, 3821.
- [24] A. K. Kyaw, D. H. Wang, V. Gupta, W. L. Leong, L. Ke, G. C. Bazan, A. J. Heeger, *ACS Nano* **2013**, *7*, 4569.
- [25] Y. Liu, C. C. Chen, Z. Hong, J. Gao, Y. Yang, H. Zhou, L. Dou, G. Li, Y. Yang, *Sci. Rep.* **2013**, *3*, 3356.
- [26] K. Sun, Z. Xiao, S. Lu, W. Zajaczkowski, W. Pisula, E. Hanssen, J. M. White, R. M. Williamson, J. Subbiah, J. Ouyang, A. B. Holmes, W. W. Wong, D. J. Jones, *Nat. Commun.* **2015**, *6*, 6013.
- [27] B. Kan, M. Li, Q. Zhang, F. Liu, X. Wan, Y. Wang, W. Ni, G. Long, X. Yang, H. Feng, Y. Zuo, M. Zhang, F. Huang, Y. Cao, T. P. Russell, Y. Chen, *J. Am. Chem. Soc.* **2015**, *137*, 3886.

- [28] B. Kan, Q. Zhang, M. Li, X. Wan, W. Ni, G. Long, Y. Wang, X. Yang, H. Feng, Y. Chen, *J. Am. Chem. Soc.* **2014**, *136*, 15529.
- [29] J. Liu, B. Walker, A. Tamayo, Y. Zhang, T. Q. Nguyen, *Adv. Funct. Mater.* **2012**, *23*, 47.
- [30] H. Buerckstuemmer, E. V. Tulyakova, M. Deppisch, M. R. Lenze, N. M. Kronenberg, M. Gsaenger, M. Stolte, K. Meerholz, F. Wuerthner, *Angew. Chem., Int. Ed.* **2011**, *50*, 11628.
- [31] R. Fitzner, E. Mena-Osteritz, A. Mishra, G. Schulz, E. Reinold, M. Weil, C. Körner, H. Ziehlke, C. Elschner, K. Leo, M. Riede, M. Pfeiffer, C. Urich, P. Bäuerle, *J. Am. Chem. Soc.* **2012**, *134*, 11064.
- [32] G. Long, X. Wan, B. Kan, Z. Hu, X. Yang, Y. Zhang, M. Zhang, H. Wu, F. Huang, S. Su, Y. Cao, Y. Chen, *ChemSusChem* **2014**, *7*, 2358.
- [33] G. Wei, S. Wang, K. Sun, M. E. Thompson, S. R. Forrest, *Adv. Energy Mater.* **2011**, *1*, 184.
- [34] K. R. Graham, P. M. Wieruszewski, R. Stalder, M. J. Hartel, J. Mei, F. So, J. R. Reynolds, *Adv. Funct. Mater.* **2012**, *22*, 4801.
- [35] S. Loser, C. J. Bruns, H. Miyauchi, R. P. Ortiz, A. Facchetti, S. I. Stupp, T. J. Marks, *J. Am. Chem. Soc.* **2011**, *133*, 8142.
- [36] J. Min, Y. N. Luponosov, Z. G. Zhang, S. A. Ponomarenko, T. Ameri, Y. Li, C. J. Brabec, *Adv. Energy Mater.* **2014**, *4*, 1400816.
- [37] H. Qin, L. Li, F. Guo, S. Su, J. Peng, Y. Cao, X. Peng, *Energy Environ. Sci.* **2014**, *7*, 1397.
- [38] J. Rivnay, S. C. B. Mannsfeld, C. E. Miller, A. Salleo, M. F. Toney, *Chem. Rev.* **2012**, *112*, 5488.
- [39] Y. Huang, E. J. Kramer, A. J. Heeger, G. C. Bazan, *Chem. Rev.* **2014**, *114*, 7006.
- [40] F. Liu, Y. Gu, X. Shen, S. Ferdous, H. W. Wang, T. P. Russell, *Prog. Polym. Sci.* **2013**, *38*, 1990.
- [41] W. Chen, M. P. Nikiforov, S. B. Darling, *Energy Environ. Sci.* **2012**, *5*, 8045.
- [42] P. Müller-Buschbaum, *Adv. Mater.* **2014**, *26*, 7692.
- [43] S. Mukherjee, C. M. Proctor, G. C. Bazan, T. Q. Nguyen, H. Ade, *Adv. Energy Mater.* **2015**, *5*, 1500877.
- [44] W. Li, K. H. Hendriks, A. Furlan, W. Roelofs, M. M. Wienk, R. A. Janssen, *J. Am. Chem. Soc.* **2013**, *135*, 18942.
- [45] M. Scarongella, J. De Jonghe-Risse, E. Buchaca-Domingo, M. Causa, Z. Fei, M. Heeney, J. E. Moser, N. Stingelin, N. Banerji, *J. Am. Chem. Soc.* **2015**, *137*, 2908.
- [46] E. Buchaca-Domingo, K. Vandewal, Z. Fei, S. E. Watkins, F. H. Scholes, J. H. Bannock, J. C. de Mello, L. J. Richter, D. M. DeLongchamp, A. Amassian, M. Heeney, A. Salleo, N. Stingelin, *J. Am. Chem. Soc.* **2015**, *137*, 5256.
- [47] D. Murthy, A. Melianas, Z. Tang, G. Juska, K. Arlauskas, F. Zhang, L. D. Siebbeles, O. Inganas, T. J. Savenije, *Adv. Funct. Mater.* **2013**, *23*, 4262.
- [48] A. Maurano, R. Hamilton, C. G. Shuttle, A. M. Ballantyne, J. Nelson, B. O'Regan, W. Zhang, I. McCulloch, H. Azimi, M. Morana, C. J. Brabec, J. R. Durrant, *Adv. Mater.* **2010**, *22*, 4987.
- [49] D. Fernandez, A. Viterisi, J. William Ryan, F. Gispert-Guirado, S. Vidal, S. Filippone, N. Martin, E. Palomares, *Nanoscale* **2014**, *6*, 5871.
- [50] D. A. Vithanage, E. Wang, Z. Wang, F. Ma, O. Inganas, M. R. Andersson, A. Yartsev, V. Sundstrom, T. Pascher, *Adv. Energy Mater.* **2014**, *4*, 1301706.
- [51] J. Guo, H. Ohkita, H. Benten, S. Ito, *J. Am. Chem. Soc.* **2010**, *132*, 6154.
- [52] I. A. Howard, R. Mauer, M. Meister, F. Laquai, *J. Am. Chem. Soc.* **2010**, *132*, 14866.
- [53] F. Etzold, I. A. Howard, N. Forler, D. M. Cho, M. Meister, H. Mangold, J. Shu, M. R. Hansen, K. Müllen, F. Laquai, *J. Am. Chem. Soc.* **2012**, *134*, 10569.
- [54] R. A. Marsh, J. M. Hodgkiss, S. bert-Seifried, R. H. Friend, *Nano Lett.* **2010**, *10*, 923.
- [55] Z. Guo, D. Lee, R. D. Schaller, X. Zuo, B. Lee, T. Luo, H. Gao, L. Huang, *J. Am. Chem. Soc.* **2014**, *136*, 10024.
- [56] a) J. M. Szarko, B. S. Rolczynski, S. J. Lou, T. Xu, J. Strzalka, T. J. Marks, L. Yu, L. X. Chen, *Adv. Funct. Mater.* **2014**, *24*, 10; b) M. Gruber, M. Rawolle, J. Wagner, D. Magerl, U. Hörmann, J. Perlich, S. V. Roth, A. Opitz, F. Schreiber, P. Müller-Buschbaum, W. Brütting, *Adv. Energy Mater.* **2013**, *3*, 1075.
- [57] J. Kniepert, I. Lange, N. J. van der Kaap, L. Koster, D. Neher, *Adv. Energy Mater.* **2014**, *4*, 1301401.
- [58] S. Albrecht, W. Schindler, J. Kurpiers, J. Kniepert, J. C. Blakesley, I. Dumsch, S. Allard, K. Fostiropoulos, U. Scherf, D. Neher, *J. Phys. Chem. Lett.* **2012**, *3*, 640.
- [59] K. Vandewal, S. Albrecht, E. T. Hoke, K. R. Graham, J. Widmer, J. D. Douglas, M. Schubert, W. R. Mateker, J. T. Bloking, G. F. Burkhard, A. Sellinger, J. M. J. Fréchet, A. Amassian, M. K. Riede, M. D. McGehee, D. Neher, A. Salleo, *Nat. Mater.* **2014**, *13*, 63.
- [60] H. C. Liao, C. S. Tsao, Y. T. Shao, S. Y. Chang, Y. C. Huang, C. M. Chuang, T. H. Lin, C. Y. Chen, C. J. Su, U. Jeng, Y. F. Chen, W. F. Su, *Energy Environ. Sci.* **2013**, *6*, 1938.
- [61] C. M. Liu, Y. W. Su, J. M. Jiang, H. C. Chen, S. W. Lin, C. J. Su, U. Jeng, K. H. Wei, *J. Mater. Chem. A* **2014**, *2*, 20760.
- [62] H.-J. Jhuo, S.-H. Liao, Y.-L. Li, P.-N. Yeh, S.-A. Chen, W.-R. Wu, C.-J. Su, J.-J. Lee, N. L. Yamada, U. Jeng, *Adv. Funct. Mater.* **2016**, *26*, 3094.
- [63] W.-R. Wu, U. Jeng, C. J. Su, K. H. Wei, M. S. Su, M. Y. Chiu, C. Y. Chen, W. B. Su, C. H. Su, A. C. Su, *ACS Nano* **2011**, *5*, 6233.
- [64] G. F. Burkhard, E. T. Hoke, M. D. McGehee, *Adv. Mater.* **2010**, *22*, 3293.
- [65] P. J. Brown, D. S. Thomas, A. Köhler, J. S. Wilson, J. S. Kim, C. M. Ramsdale, H. Sirringhaus, R. H. Friend, *Phys. Rev. B* **2003**, *67*, 064203.
- [66] C. Deibel, T. Strobel, V. Dyakonov, *Adv. Mater.* **2010**, *22*, 4097.
- [67] a) G. Grancini, D. Polli, D. Fazzi, J. Cabanillas-Gonzalez, G. Cerullo, G. Lanzani, *J. Phys. Chem. Lett.* **2011**, *2*, 1099; b) I. Constantinou, T.-H. Lai, H.-Y. Hsu, S.-H. Cheung, E. D. Klump, K. S. Schanze, S.-K. So, F. So, *Adv. Electron. Mater.* **2015**, *1*, 201500167.
- [68] D. Rauh, C. Deibel, V. Dyakonov, *Adv. Funct. Mater.* **2012**, *22*, 3371.
- [69] W. Shockley, W. T. Read, *Phys. Rev.* **1952**, *87*, 835.
- [70] B. Wu, X. Y. Wu, C. Guan, K. F. Tai, E. K. L. Yeow, H. J. Fan, N. Mathews, T. C. Sum, *Nat. Commun.* **2013**, *4*, 2004.
- [71] P. G. W. Blom, V. G. D. Mihaletchi, L. G. J. Koster, D. G. E. Markov, *Adv. Mater.* **2007**, *19*, 1551.
- [72] G. Long, B. Wu, X. Yang, B. Kan, Y. C. Zhou, L. C. Chen, X. Wan, H. L. Zhang, T. C. Sum, Y. Chen, *ACS Appl. Mater. Interfaces* **2015**, *7*, 21245.
- [73] G. G. Malliaras, J. R. Salem, P. J. Brock, C. Scott, *Phys. Rev. B* **1998**, *58*, R13411.
- [74] J. D. Chai, M. Head-Gordon, *Phys. Chem. Chem. Phys.* **2008**, *10*, 6615.
- [75] Gaussian 09, Revision B.01, Gaussian, Inc., Wallingford CT, 2010, see the Supporting Information for full citation.
- [76] U. Jeng, C. H. Su, C. J. Su, K. F. Liao, W. T. Chuang, Y. H. Lai, J. W. Chang, Y. J. Chen, Y. S. Huang, M. T. Lee, K. L. Yu, J. M. Lin, D. G. Liu, C. F. Chang, C. Y. Liu, C. H. Chang, K. S. Liang, *J. Appl. Crystallogr.* **2010**, *43*, 110.